HHS Public Access

Author manuscript

*ACS Appl Mater Interfaces*. Author manuscript; available in PMC 2023 August 05.

Published in final edited form as:

*ACS Appl Mater Interfaces*. 2023 January 11; 15(1): 1798–1807. doi:10.1021/acsami.2c16741.

# A Highly Sensitive, Stretchable and Robust Strain Sensor based on Crack Propagation and Opening

**Shuang Wu**[1], **Katherine Moody**[1], **Abhiroop Kollipara**[1], **Yong Zhu**[1,2,3]

[1]Department of Mechanical and Aerospace Engineering, North Carolina State University, Raleigh, North Carolina 27695, USA

[2]Department of Materials Science and Engineering, North Carolina State University, Raleigh, North Carolina 27695, USA

[3]Joint Department of Biomedical Engineering, University of North Carolina-Chapel Hill and NC State University, Chapel Hill, North Carolina 27599, USA

## Abstract

Soft and stretchable strain sensors have been attracting significant attention. However, the tradeoff between the sensitivity (gauge factor) and the sensing range has been a major challenge. In this work, we report a soft stretchable strain sensor with an unusual combination of high sensitivity, large sensing range, and high robustness. The sensor is made of silver nanowire network embedded below the surface of an elastomeric matrix (e.g., polydimethylsiloxane). Periodic mechanical cuts are applied to the top surface of the sensor, changing the current flow from uniformly across the sensor to along the conducting path defined by the open cracks. Both experiment and finite element analysis are conducted to study the effect of the cut depth, cut length, and pitch between the cuts. The stretchable strain sensor can be integrated into wearable systems for monitoring of physiological functions and body motions associated with different levels of strains, such as blood pressure and lower back health. Finally, a soft 3D touch sensor

Corresponding Author yzhu7@ncsu.edu.

Author contributions

S.W. and Y.Z. conceived the idea and designed the experiments and simulations. S.W. conducted the experiments, simulations and data analysis, K.M. helped with the data analysis, A.K. helped with the electronics for data acquisition. S.W. and Y.Z. wrote the manuscript with inputs from all the authors.

Supporting Information.

The Supporting Information is available free of charge on the ACS via the Internet at http://pubs.acs.org. Additional figure including Resistance change of AgNW/PDMS composites with increase of the number of cuts; SEM images of the cut surfaces of AgNW/PDMS composite with AgNW densities of (a) 0.1 and (b) 0.5 mg/cm$^{-1}$; Force-displacement curves of a razor blade pushing into the AgNW/PDMS composites of different AgNW densities; Electromechanical simulation of the strain sensor. a, Schematic plot of the sensor. b, Electrical current densities of the sensor at zero and 15% strain. c, Comparison between FEA and experimental results of the sensor with $p/w$ = 0.1, 0.2 and 0.3; a, Crack length with respect to applied strain. b, Relative resistance changes with respect to crack length; FEA Simulation of the strain distribution of the sensor under 30% applied strain; Resistance changes of the AgNW/PDMS composite under 5% and 6% stretching-and-unloading; a, Photograph of the Arduino Bluetooth board for the wearable strain sensing system (with custom-made voltage divider circuit). b, Diagram showing the design of the Bluetooth board and voltage divider circuit; Calibration of the sensors integrated with athletic fabrics. a, Photographs of the sensor/fabric setup with fiducial marker dots on the skin. b, Comparison between the strains measured by the sensor/fabric and by the fiducial markers using a camera; Calibration of the shear strain sensor enabled by two sensors. a, Photograph of a shear strain sensing system with two orthogonal strain sensors. b, The resistance change of the sensors in horizontal direction and vertical direction with a vertical shear strain applied; Real-time control of an airplane in a video game with the functions of turning left, turning right, acceleration, and deceleration (movie1); Robotic sensing of grabbing, lifting and dropping a glass of water (movie2).

that tracks both normal and shear stresses is developed for human-machine interfaces and tactile sensing for robotics.

## Graphical Abstract

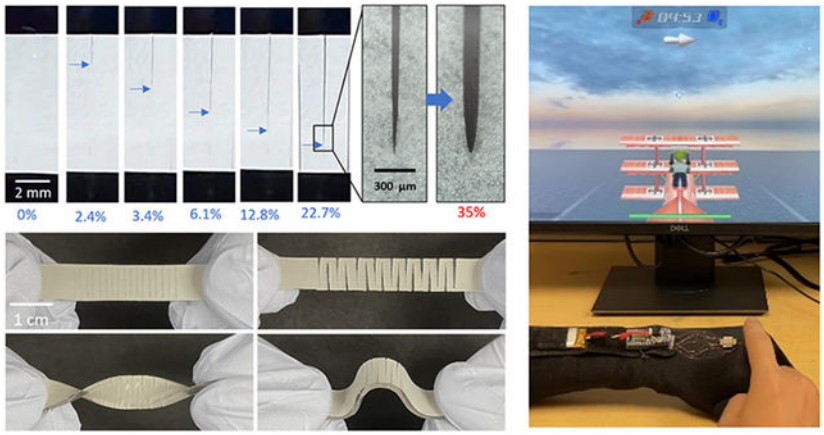


### Keywords

Strain sensor; silver nanowires; crack; stretchable electronics; health monitoring; human-machine interface

## Introduction

Soft and stretchable strain sensors have been attracting significant interests because of their wide applications in wearable electronics for physiological monitoring and motion tracking[1-12], human machine interfaces[13-16], and soft robotics[17-21]. A variety of nanocomposite materials have been explored for use in soft and stretchable sensors, including carbon nanotubes (CNTs)[22-24], graphene[25-27],metal nanoparticles[28], magnetic nanoparticles[29-33], and metal nanowires[10, 34-37]. In stretchable strain sensors, these materials typically exist in the form of three-dimensional percolation network embedded in a polymer matrix. Stretching the composite matrix decreases the percolation density, resulting in decreased electrical conductivity. In parallel, structural design strategies have been used to significantly reduce the effective strain on the conducting materials, leading to better stretchability. A number of mechanically guided structural designs have been reported, such as wrinkles[38-39], serpentines[40], spirals/helices[41-42], and kirigami[43-44] and auxetic metamaterials[45].

Recent advancements in wearable technology and soft robotics have led to the development of new stretchable strain sensors with enhanced sensing performances, such as large gauge factor (GF), large strain range, high linearity, better conformability, and robustness[3]. However, tradeoffs between these performances have been a major challenge for almost all existing strain sensors. For example, a Pt/polyurethane acrylate (PUA) composite resistive sensor with surface crack design has been reported with an ultrahigh GF of 2000, yet a strain range of only 2%[46], which is low for most applications such as body motion tracking.

Another crack-based strain sensor also shows good sensitivity (GF=9400) but with small sensing range (<3%)[20]. These examples illustrate promising potential of measuring contact resistance change between crack surfaces for strain sensing. However, using well-defined, periodic mechanical cuts in soft materials to control the crack propagation and opening has not been explored. On the other hand, A highly stretchable capacitive strain sensor enabled by wrinkled gold films showed a strain range of 250% but a GF of only 0.9[47], which limits the sensing capabilities for small strains. Some researchers have also developed sensors with large strain range (450% to 500%) and high sensitivity (GF of 67.7 to 10000)[38, 48]. But they typically showed a nonlinear response (smaller GF at low strains and large GF at higher strains).

For monitoring of human physiology and motion, the skin strain ranges from less than 1% to over 50%[49]. Typically, one sensor is used to detect subtle strains associated with physiological functions (e.g., blood pulse and respiration), while another for large strains associated with bending of body parts (e.g., knee, elbow, and back). It would be of great interest to develop one strain sensor, in the form of either a skin patch or a textile band, which can capture the full range of strains on human skin and can thus be attached onto different parts of the body[50]. For monitoring certain diseases, it is indeed critical to accurately measure a wide range of strains. For example, in the case of Parkinson's disease, the symptoms include resting tremor, rigid muscles, bradykinesia and sometimes a combination of above[51-53]. The sensors must be sensitive enough for monitoring small tremors while maintaining a large sensing range to measure joint movements. Moreover, soft strain sensors may encounter adverse conditions during operation, such as impacts and over-extension, where the applied strain could substantially exceed the sensing range. Therefore, it is of important relevance to develop a stretchable strain sensor with high sensitivity, large sensing range, and high robustness (i.e., surviving over-strain and repeatability), which remains a significant challenge.

This work reports a soft stretchable strain sensor that can achieve all three goals by combining the use of nanomaterials with a novel structural design strategy. The sensor is made of silver nanowire (AgNW) network embedded below the surface of polydimethylsiloxane (PDMS). Periodic mechanical cuts are applied to the top surface of the AgNW/PDMS composite, changing the current flow from uniformly across the sensor to along the conducting path defined by the open cracks. Under the applied strain, the resistance increases as the crack propagates, but remains constant as the crack reaches the cut length and exhibits tip blunting. Both regions are totally reversible and repeatable. Both experiment and finite element analysis have been conducted to study the effect of the cut depth, cut length, and pitch between the cuts, highlighting excellent tunability of the GF, sensing range, and reversible range of the sensor. The stretchable strain sensor was integrated into two systems for wearable monitoring of blood pressure and lower back health, demonstrating the capabilities for small-strain and large-strain sensing, respectively. Finally, a soft 3D touch sensor that tracks both normal and shear stresses was developed for human-machine interfaces and tactile sensing for robotics.

## Results

Fig. 1a shows the fabrication process of the AgNW strain sensor with the surface crack design. The AgNW solution was drop-casted on a sacrificial substrate and then heated to evaporate the solvent. Then liquid PDMS precursor was mixed thoroughly and spin-coated on top of the AgNW network. The AgNW/PDMS composite was cured at 70°C for 1 hour. The cured sample was then peeled off from the substrate with the AgNW network embedded below the surface of the PDMS matrix[54]. Then the composite film was cut from the AgNW side using a mechanical cutter, cutting through the AgNW/PDMS composite into the pure PDMS layer (Fig. 1b). The AgNW/PDMS layer was cut into a zigzag-shaped pattern. Finally, Cu lead wires were attached to the two ends of the pattern by silver epoxy.

Fig. 1b shows the electrical models of the samples during and after the mechanical cuts. $2R_0$ is the initial resistance of the sample. As the razor blade cuts through the AgNW/PDMS composite, AgNWs along the cutting path are broken and pushed in. After retrieval of the blade, the AgNWs on the two cutting surfaces form a physical contact with the contact resistance of $R_c$. The SEM image shows the cross section view of the cutting surface.

Fig. S1 shows the resistance changes of the AgNW/PDMS composite samples of different AgNW densities with respect to the number of cuts. All samples showed a gradual increase of resistance with the increasing number of cuts. The sample with AgNW density of 0.5 mg/cm$^{-1}$ yielded a minimum resistance change of only 15.3% after 5 cuts while the sample with AgNW density of 0.1 mg/cm$^{-1}$ showed a resistance change of 321.9%. This can be explained by the different fracture mechanisms in the two cases. From Fig. S2 a, the low-density sample showed a clean-cut surface with AgNWs along the cutting path broken and sticking out. The depth of the conductive contact surface in this case was ~3 μm. However, for the sample with high-density AgNW network, the AgNW/PDMS composite was deformed and pushed inwards. In the case of 0.5 mg/cm$^{-1}$, the depth of the conductive contact surface was over 13 μm (Fig. S2 b). This large contact area enabled the resistance change to be as low as 5% after each cut. In the rest of this work, 0.5 mg/cm$^{-1}$ AgNW density was chosen for all the strain sensors due to their stable contact resistances. The force-displacement curves of the samples with different AgNW densities are shown in Fig. S3. It can be seen that a higher cutting force is required to break through the composite layer with a higher AgNW density. Fig. 1c shows the crack-based strain sensor under twisting, bending, and stretching (30% strain). With increase of the applied strain, the crack gradually propagated, which caused $R_c$ to increase; inversely, with decrease of the applied strain, the crack retracted leading to decrease of $R_c$. The electromechanical response of the sensor is highly reversible under cyclic loading (to be discussed in Fig. 2).

To study the electrical performance of the sensors for different geometrical designs, we defined three major geometrical parameters – ratio of the cut depth to the sample thickness $d_c/t$, ratio of the pitch between the cracks to the specimen width $p/w$, and ratio of the cut length to the specimen width $l_c/w$ (Fig. 2a). Fig. 2b shows the resistance change of the crack-based sensor as a function of the applied strain. The resistance change curve can be divided into two regions, a sensing region where the resistance increases linearly with the increasing strain, and a plateau region. The crack propagation/opening process

was observed in-situ under an optical microscope, while the resistance was measured simultaneously. 1,000 stretching/unloading cycles (1.2 mm/s) were applied to show the excellent repeatability of the sensor for long term use (Fig. 2c). Fig. S4 shows the stress-strain curve and the resistance change of the sensor under different strain rate (1.2 mm/s, 0.6 mm/s and 0.3 mm/s), which shows good repeatability in all cases.

The optical images in the sensing range (Fig. 2d ①-⑨) show the gradual propagation of a single crack. In this range, the current flow follows the cut guided path. As a result, the resistance of the sensor increases with the crack propagating. However, this resistance change stops when the crack is fully open, i.e., the two crack surfaces lose contact, as shown in the magnified optical image (Fig. 2d ⑩). Fig. S5 also shows the relationship between the applied strain, the crack length, and the relative resistance change.

The sensor can be further stretched without resistance change, as shown in the plateau region in Fig. 2b. In this case, the crack reaches the full cut length. Under the applied strain, the crack further opens with the crack tip blunting but not advancing beyond the cut length. This plateau region is important as it can protect the sensors from failing due to unexpected large strains. Here we define this reversible range by the combination of the sensing region and the plateau region. Beyond the plateau region, the local strain in front of the crack tip would cause irreversible sliding in the AgNW network, leading to overall irreversible resistance change. If the applied strain further increases, the crack tip could propagate beyond the cut length, causing more serious irreversibility in the resistance.

Fig. 3a shows the relative resistance changes of three samples with $d_c/t$ of 1/8, 1/4, and 1/2, with $p$, $w$ and $l_c$ remaining the same ($p/w = 0.2$, $l_c/w = 0.9$). The three cases showed the same GF of 81.5 and the linear sensing region gradually increased with the decreasing cut depth. This is due to the difference in the crack propagation rate for the different cut depths. The shallower the cuts, the larger the applied strain to complete the crack propagation and opening. The plateau region gradually decreased with the decreasing cut depth (Fig. 2d).

In Fig. S6, finite element analysis (FEA) (ABAQUS, version 2017) was conducted to simulate the crack propagation and opening behavior of the AgNW/PDMS composite. With the introduction of mechanical cuts, the effective modulus reduces. With larger $d_c/t$, the effective modulus reduces more. Similarly, with smaller p/w and larger $l_c/w$, the effective modulus drop of the sensor increases (Fig. S7). The maximum strain in the AgNW/PDMS layer lies ahead of the crack tip during stretching. When it exceeds a critical strain $\varepsilon_c$, we assume that the irreversible sliding in the AgNW network occurs, causing irreversible damage in the AgNW network and hence the irreversible resistance of the sensor. The critical strain on AgNW/PDMS composite was measured to be $\varepsilon_c = 5\%$ under tension. As shown in Fig. S8, the resistance of the AgNW beyond 5% tensile strain was irreversible. Here we characterize the reversible range by the applied strain when the maximum strain at the crack tip of the AgNW/PDMS layer reaches 5%. FEA simulations found the reversible ranges of 31.4%, 38.3%, and 45.1% for $d_c/t$ of 1/8, 1/4, and 1/2, respectively (marked with cross marks in Fig. 3a). To guarantee the reversibility of the sensor, the applied strain remains below the reversible range, which is much smaller than the breaking strain; above the breaking strain the crack would further advance beyond the initial cut length. To sum up,

with different cut depths, a tradeoff exists between the sensing range and the reversible range while having the same GF.

Fig. 3b demonstrates the effect of $p/w$ on the relative resistance change, while $d_c/t$ and $l_c/w$ stayed as 1/8 and 0.9, respectively. With the decrease of $p/w$ from 0.3 to 0.1, the GF increased from 81.5 to 290.1. With a smaller $p/w$, the pitch between the cracks decreases while the number of the cut paths increases, thus the overall resistance change can increase dramatically. Fig. 3c shows a slight increase of the resistance change with the increasing $l_c/w$ while keeping $d_c/t$ = 1/8 and $p/w$ = 0.3, because the final "neck" of the conducting path after the crack propagation completes is narrower with the increase of $l_c/w$. These results on the three parameters, $d_c/t$, $p/w$ and $l_c/w$, demonstrated excellent tunability of the GF, sensing range, and reversible range of the sensor.

Fig. 4 shows a benchmark comparison between the present work and the reported stretchable strain sensors enabled by different sensing mechanisms, including resistive sensors[22-23, 26, 28, 35, 46] capacitive sensors[10-11] and piezoelectric sensors[55]. Of note is that the selected strain sensors in the map all showed high linearity and reversibility. In general, a tradeoff exists between the GF and the sensing range for stretchable strain sensors. From this map, it can be seen that the present work yields a large GF = 290.1 with a decent strain sensing range (22%), exceeding the envelop defined by the reported stretchable strain sensors. After integration on stretchable substrates (e.g., athletic tape to be discussed later), the stretchability of the sensor can be further enhanced.

A coupled electromechanical FEA model was built (COMSOL Multiphysics 5.6) to understand the resistance change of the strain sensor under stretching (Fig. S9 a). The AgNW/PDMS composite was modeled as an isotropic conductive material and the contact resistance between the two crack surfaces was considered to be dependent on the crack opening. When the distance between the two surfaces exceeds a critical value, the contact resistance drops from an initial value to zero. This model can simulate the gradual propagation and opening of the crack. Material parameters used in the simulation such as sheet resistance of the AgNW/PDMS composite and contact resistance were measured (e.g., in the case of NW density of 0.5 mg/cm$^2$, sheet resistance of the AgNW/PDMS composite is 0.25 Ω sq$^{-1}$ and contact resistance per unit length is 1.6 Ω cm$^{-1}$). By taking the integral of the ECD along the conducting path we can calculate the resistance change with respect to the applied strain. The FEA results agreed well with the experimental results of different $p/w$ ratios (Fig. S9 b). Fig. S9 c shows the simulated electrical current density (ECD) field of the strain sensor before and after stretching. With the increase of the applied strain, the ECD field shows a transition from uniform current flow (across the closed cracks) to current flow along the conducting path defined by the open cracks. This model could predict the performance of the sensors with even more complicated cutting patterns, providing valuable guidance to the sensor design.

To demonstrate the versatile applicability of our strain sensors for monitoring human motions, we first applied the sensors on the wrist to detect the pulse wave, which represents one of the most delicate strain signals on human skin. Fig. 5a shows the setup consisting of a rubber band with a slot filled with the strain sensor. The rubber band was fastened on

the wrist to secure the strain sensor against the pulsing area. When the blood pumps through the vein, the two ends of the strain sensor are fixed by the rubber band while the middle is bent and stretched. Then the cracks are opened on the top surface. The red curve in Fig. 5b shows the pulse wave captured from the radial artery on the wrist. Similarly, another strain sensor can be placed on the brachial artery on the arm, recording another pulse wave simultaneously (black curve in Fig. 5b). By measuring the distance between the two pulse areas and taking the average of the time gap between peaks of the two pulse waves, the averaged pulse wave velocity (PWV) can be measured, based on which the blood pressure (BP) can be obtained following[56]

$$BP = \alpha PWV^2 + \beta$$

where $\alpha = 0.18\,\text{kPa} \cdot \text{s}^2 \cdot \text{m}^{-2}$ and $\beta = 2.7\,\text{kPa}$[56]. Taking PWV = 7.5 m/s as measured from Fig. 5b, the BP was calculated to be 12.8 kPa, which equals 96.2 mmHg.

The other demonstration aimed to monitor the large strains on the lower back, which is a critical signal for metabolic syndrome and spine issues[57-58]. The sensor was integrated onto an athletic tape by fixing the two ends of the sensor on the tape using a PDMS precursor (Fig. 5c inset). Two sensor/tape setups were attached on the lower back side by side in parallel with the spine. An Arduino Bluetooth board/tape was attached in the middle area of the lower back to collect and transmit the sensing signals to a smart phone. The details of the Bluetooth board design are shown in Fig. S10, where $R_0$ is the dummy resistor and $R_1$-$R_6$ are the six available channels (only two used in this demonstration). The subject started from a sitting-straight posture and leaned forward three times with increasing degree. Then the subject leaned forward while tilting rightward and leftward. Fig. 5c shows the measured strain signals of the two sensor/tape setups. When leaning forward, both sensors responded with resistance increases. While leaning forward and tilted sideways, the resistance of the sensor in the corresponding side remained nearly constant and the one at opposite side increased substantially. The calibration of the sensor/fabric setup is shown in Fig. S11 a. Four fiducial markers were drawn alongside the crack-based sensors on the skin for the purpose of validation. The results measured by the sensor and by the fiducial markers showed an excellent agreement (Fig. S11 b). Of nots is that by integrating the strain sensor with a stretchable athletic tape, the overall stretchability of the sensor/tape setup can be increased on demand according to the need of the applications. In the setup, the strain distributions in the sensor/tape region and the pure tape are different. Due to the larger Young's modulus, the sensor/tape region has a smaller strain than the pure tape region. By adjusting the modulus ratio, a sensor/tape setup can be easily integrated for wearable applications with large stretchability, e.g., motion tracking on human joints.

Finally, besides wearable personal health monitoring, the senor can be applied for human-machine interfaces and robotics. Fig. 6a shows the schematic diagram of an integrated 3D touch sensor. The two solid AgNW/PDMS composite in the middle form a capacitive pressure sensor that detects normal pressure[8], while the four surrounding AgNW/PDMS composite ribbons with the surface crack design (CS1, CS2, CS3 and CS4) work as shear stress sensors. The pressure sensor was connected to a capacitance evaluation board and the

shear sensors were connected to a multichannel resistance meter (Fig. 6b). Fig. S12 shows the calibration results of the shear sensors. When a shear force is applied in the middle area, one shear stress sensor away from the moving direction is stretched. The cracks in the stretched sensor open, resulting in a resistance increase. Fig. 6c shows excellent decoupled responses when shear forces in four directions were applied sequentially. Fig. 6d shows real-time control of an airplane in a video game with the functions of turning left, turning right, acceleration, and deceleration. This device illustrates a promising potential in virtual reality and soft human-machine interfaces.

Fig. 6e shows the sensor applied for tactile sensing. The sensor was integrated on the fingertip of a glove and then used for grasping a glass of water (200 g). Fig. 6f captures the shear and normal strains of two trials with different lifting and dropping speeds. When the glass of water was grabbed but not lifted, the capacitance of the middle sensor increased while the resistance of the shear sensor remained constant. During lifting, the shear strain increased to overcome the gravity of the glass of water. When dropping the water on the table, the shear strain decreased to zero followed by the normal strain decreasing to zero. Note that the shear strain curve of the first trial showed a period of overshot because the fast lifting required extra shear force for acceleration. However, the second trial was 3 times slower in the lifting speed and the shear strain showed no obvious overshot. This application demonstrated the great potential for tactile sensing for robotics.

## Conclusions

In summary, this work reported simple, facile fabrication of a versatile soft stretchable strain sensor for wearable applications. We designed and fabricated a AgNW/PDMS composite based strain sensor with simple mechanical cuts into the top surface. Under the applied strain, the resistance increased as the crack propagated (the sensing range), but remained constant as the crack reached the cut length (the reversible range). Under further loading, the local strain in front of the crack tip would cause irreversible sliding in the AgNW network, leading to irreversible resistance change. The effect of the cut depth, cut length, and pitch between the cuts, were studied to optimize the sensor performances. This sensor overcame the limitation of most existing strain sensors and offered unprecedented combination of GF, strain sensing range and robustness (under over-strain and 1,000 repeated loading cycles). A large GF of 290.1 was achieved with a sensing range over 22%. FEA was conducted to validate the electrical performance and predict the mechanical damage, agreeing very well with the experimental results. As demonstrations, the stretchable strain sensor was integrated into several systems for wearable monitoring of blood pressure and lower back health and 3D touch sensing that tracks both compressive and shear stresses simultaneously, illustrating the promising potential for a range of applications including personal human health monitoring, human-machine interfaces, and tactile sensing for robotics.

## Methods

### Synthesis of AgNW solution.

First, 60 mL of a 0.147 M PVP (MW ~ 40000, Sigma-Aldrich) solution in EG was added to a flask, to which a stir bar was added; the solution was then suspended in an oil bath

(temperature 151.5 °) and heated for 1 h under magnetic stirring (150 rpm). Then 200 μL of a 24 M $CuCl_2$ ($CuCl_2 \cdot 2H_2O$, 99.999+%, Sigma-Aldrich) solution in EG was injected into the PVP solution. The mixture solution was then injected with 60 mL of a 0.094 M $AgNO_3$ (99+%, Sigma-Aldrich) solution in EG[59].

### Fabrication of the strain sensor.

The AgNW solution was drop-casted on a plasma treated glass slide, which was placed onto a hot plate at 50 °C to evaporate the solvent. After the solvent was evaporated, liquid PDMS (SYLGARD 184, DOW Inc.) with a weight ratio of 10:1 was mixed thoroughly and dropped on top of the AgNW film in a rectangular mold. The AgNW/PDMS composite was cured at 70°C for 1 hour[10, 60]. The cured sample was then cut from the top surface using a mechanical cutter (silhouette CAMEO). Cu wires were attached to the two outer ends of the sample by silver epoxy (MG Chemicals).

### Fabrication of the 3D touch sensor.

First, the as-synthesized AgNWs were drop casted onto a sacrificial substrate. The AgNWs together with the sacrificial substrate were then laser cut into a cross-shaped pattern. The pattern defined the conductive area into five regions: a square region in the middle (one electrode of the capacitive sensor) and four surrounding rectangular regions (for making the crack-based resistive strain sensors). PDMS was poured on top of the five pieces of AgNWs and then baked at 70°C for 1 hour. After curing of PDMS, the sample was flipped over and cut on the designed areas using the mechanical cuter. Another piece of AgNW/PDMS composite was glued on top of the middle square region to compose a capacitive pressure sensor. Then all five parts of the touch sensor were wired with copper wires.

### Video game control using the 3D touch sensor.

To transmit the resistance signal, we used an ARDUINO board (nano 33) and built a simple voltage divider circuit with four dummy resistors. Each channel of the touch sensor was connected to a dummy resistor in series. The voltages across dummy resistors and crack-sensors were collected by the ARDUINO board and processed to calculate the real time resistances of the sensors in each direction. An ARDUINO code was built to read the real-time resistance values of each channel and compare to a triggering threshold $Rt$ to decide whether or not to send out a signal. For example, when the 3D touch sensor was pressed and pushed to the right direction, the left crack sensor CS3 reached a resistance increase over 20% which triggered the ARDUINO board to send out a keyboard signal ‘right arrow’. As a result, the airplane in the video game will make a right turn. Similarly, the other three crack-based sensors have been assigned to ‘left arrow’, ‘up arrow’, and ‘down arrow’. In the airplane video game, the four arrow keys represent the functions of turning left, turning right, acceleration and deceleration.

## Supplementary Material

Refer to Web version on PubMed Central for supplementary material.

## ACKNOWLEDGMENT

The authors would like to gratefully acknowledge the National Science Foundation (NSF) for the financial support under award No. 2122841.

## References

1. Lipomi DJ; Vosgueritchian M; Tee BC; Hellstrom SL; Lee JA; Fox CH; Bao Z, Skin-Like Pressure and Strain Sensors Based on Transparent Elastic Films of Carbon Nanotubes. Nat. Nanotechnol 2011, 6 (12), 788–792. [PubMed: 22020121]
2. Chung HU; Rwei AY; Hourlier-Fargette A; Xu S; Lee K; Dunne EC; Xie Z; Liu C; Carlini A; Kim DH; Ryu D; Kulikova E; Cao J; Odland IC; Fields KB; Hopkins B; Banks A; Ogle C; Grande D; Park JB; Kim J; Irie M; Jang H; Lee J; Park Y; Kim J; Jo HH; Hahm H; Avila R; Xu Y; Namkoong M; Kwak JW; Suen E; Paulus MA; Kim RJ; Parsons BV; Human KA; Kim SS; Patel M; Reuther W; Kim HS; Lee SH; Leedle JD; Yun Y; Rigali S; Son T; Jung I; Arafa H; Soundararajan VR; Ollech A; Shukla A; Bradley A; Schau M; Rand CM; Marsillio LE; Harris ZL; Huang Y; Hamvas A; Paller AS; Weese-Mayer DE; Lee JY; Rogers JA, Skin-Interfaced Biosensors for Advanced Wireless Physiological Monitoring in Neonatal and Pediatric Intensive-Care Units. Nature medicine 2020, 26 (3), 418–429.
3. Amjadi M; Kyung KU; Park I; Sitti M, Stretchable, Skin-Mountable, and Wearable Strain Sensors and Their Potential Applications: A Review. Adv. Funct. Mater 2016, 26 (11), 1678–1698.
4. Kim D-H; Lu N; Ma R; Kim Y-S; Kim R-H; Wang S; Wu J; Won SM; Tao H; Islam A; Yu KJ; Kim T.-i.; Chowdhury R; Ying M; Xu L; Li M; Chung H-J; Keum H; Mccormick M; Liu P; Zhang Y; Omenetto FG; Huang Y. g.; Coleman T; Rogers JA, Epidermal Electronics. Science 2011, 333 (6044), 838–843. [PubMed: 21836009]
5. Boutry CM; Kaizawa Y; Schroeder BC; Chortos A; Legrand A; Wang Z; Chang J; Fox P; Bao Z, A Stretchable and Biodegradable Strain and Pressure Sensor for Orthopaedic Application. Nat. Electron 2018, 1 (5), 314–321.
6. Libanori A; Chen G; Zhao X; Zhou Y; Chen J, Smart Textiles for Personalized Healthcare. Nat. Electron 2022, 5 (3), 142–156.
7. Zhou Z; Chen K; Li X; Zhang S; Wu Y; Zhou Y; Meng K; Sun C; He Q; Fan W; Fan E; Lin Z; Tan X; Deng W; Yang J; Chen J, Sign-to-Speech Translation Using Machine-Learning-Assisted Stretchable Sensor Arrays. Nat. Electron 2020, 3 (9), 571–578.
8. Amjadi M; Pichitpajongkit A; Lee S; Ryu S; Park I, Highly Stretchable and Sensitive Strain Sensor Based on Silver Nanowire–Elastomer Nanocomposite. Acs Nano 2014, 8 (5), 5154–5163. [PubMed: 24749972]
9. Cai G; Wang J; Qian K; Chen J; Li S; Lee PS, Extremely Stretchable Strain Sensors Based on Conductive Self-Healing Dynamic Cross-Links Hydrogels for Human-Motion Detection. Advanced Science 2017, 4 (2), 1600190. [PubMed: 28251045]
10. Yao S; Zhu Y, Wearable Multifunctional Sensors Using Printed Stretchable Conductors Made of Silver Nanowires. Nanoscale 2014, 6 (4), 2345–2352. [PubMed: 24424201]
11. Yao S; Vargas L; Hu X; Zhu Y, A Novel Finger Kinematic Tracking Method Based on Skin-Like Wearable Strain Sensors. IEEE Sensors Journal 2018, 18 (7), 3010–3015.
12. Yao S; Ren P; Song R; Liu Y; Huang Q; Dong J; O'Connor BT; Zhu Y, Nanomaterial-Enabled Flexible and Stretchable Sensing Systems: Processing, Integration, and Applications. Adv. Mater 2020, 32 (15), 1902343.
13. Yu Y; Nassar J; Xu C; Min J; Yang Y; Dai A; Doshi R; Huang A; Song Y; Gehlhar R, Biofuel-Powered Soft Electronic Skin with Multiplexed and Wireless Sensing for Human-Machine Interfaces. Sci. Rob 2020, eaaz7946.
14. Wang K; Yap LW; Gong S; Wang R; Wang SJ; Cheng W, Nanowire-Based Soft Wearable Human–Machine Interfaces for Future Virtual and Augmented Reality Applications. Adv. Funct. Mater 2021, 2008347.
15. Jeong J-W; Yeo W-H; Akhtar A; Norton JJS; Kwack Y-J; Li S; Jung S-Y; Su Y; Lee W; Xia J; Cheng H; Huang Y; Choi W-S; Bretl T; Rogers JA, Materials and Optimized Designs for

Human-Machine Interfaces Via Epidermal Electronics. Adv. Mater 2013, 25 (47), 6839–6846. [PubMed: 24327417]

16. Zhou W; Yao S; Wang H; Du Q; Ma Y; Zhu Y, Gas-Permeable, Ultrathin, Stretchable Epidermal Electronics with Porous Electrodes. Acs Nano 2020, 14 (5), 5798–5805. [PubMed: 32347707]
17. Lu N; Kim D-H, Flexible and Stretchable Electronics Paving the Way for Soft Robotics. Soft Rob. 2014, 1 (1), 53–62.
18. Rich SI; Wood RJ; Majidi C, Untethered Soft Robotics. Nat. Electron 2018, 1 (2), 102–112.
19. Thuruthel TG; Shih B; Laschi C; Tolley MT, Soft Robot Perception Using Embedded Soft Sensors and Recurrent Neural Networks. Sci. Rob 2019, 4 (26), eaav1488.
20. Araromi OA; Graule MA; Dorsey KL; Castellanos S; Foster JR; Hsu W-H; Passy AE; Vlassak JJ; Weaver JC; Walsh CJ; Wood RJ, Ultra-Sensitive and Resilient Compliant Strain Gauges for Soft Machines. Nature 2020, 587 (7833), 219–224. [PubMed: 33177670]
21. Wu S; Baker GL; Yin J; Zhu Y, Fast Thermal Actuators for Soft Robotics. Soft Rob. 2021, 10.1089/soro.2021.0080.
22. Yamada T; Hayamizu Y; Yamamoto Y; Yomogida Y; Izadi-Najafabadi A; Futaba DN; Hata K, A Stretchable Carbon Nanotube Strain Sensor for Human-Motion Detection. Nat. Nanotechnol 2011, 6 (5), 296–301. [PubMed: 21441912]
23. Ryu S; Lee P; Chou JB; Xu R; Zhao R; Hart AJ; Kim S-G, Extremely Elastic Wearable Carbon Nanotube Fiber Strain Sensor for Monitoring of Human Motion. Acs Nano 2015, 9 (6), 5929–5936. [PubMed: 26038807]
24. Zhu S; Sun H; Lu Y; Wang S; Yue Y; Xu X; Mei C; Xiao H; Fu Q; Han J, Inherently Conductive Poly (Dimethylsiloxane) Elastomers Synergistically Mediated by Nanocellulose/Carbon Nanotube Nanohybrids toward Highly Sensitive, Stretchable, and Durable Strain Sensors. ACS Appl. Mater. Interfaces 2021, 13 (49), 59142–59153. [PubMed: 34851617]
25. Yu X; Cheng H; Zhang M; Zhao Y; Qu L; Shi G, Graphene-Based Smart Materials. Nat. Rev. Mater 2017, 2 (9), 1–13.
26. Bae S-H; Lee Y; Sharma BK; Lee H-J; Kim J-H; Ahn J-H, Graphene-Based Transparent Strain Sensor. Carbon 2013, 51, 236–242.
27. Iqra M; Anwar F; Jan R; Mohammad MA, A Flexible Piezoresistive Strain Sensor Based on Laser Scribed Graphene Oxide on Polydimethylsiloxane. Sci. Rep 2022, 12 (1), 1–11. [PubMed: 34992227]
28. Zheng M; Li W; Xu M; Xu N; Chen P; Han M; Xie B, Strain Sensors Based on Chromium Nanoparticle Arrays. Nanoscale 2014, 6 (8), 3930–3933. [PubMed: 24132035]
29. Zhou Y; Zhao X; Xu J; Fang Y; Chen G; Song Y; Li S; Chen J, Giant Magnetoelastic Effect in Soft Systems for Bioelectronics. Nat. Mater 2021, 20 (12), 1670–1676. [PubMed: 34594013]
30. Zhao X; Zhou Y; Xu J; Chen G; Fang Y; Tat T; Xiao X; Song Y; Li S; Chen J, Soft Fibers with Magnetoelasticity for Wearable Electronics. Nat Commun 2021, 12 (1), 1–11. [PubMed: 33397941]
31. Chen G; Zhao X; Andalib S; Xu J; Zhou Y; Tat T; Lin K; Chen J, Discovering Giant Magnetoelasticity in Soft Matter for Electronic Textiles. Matter 2021, 4 (11), 3725–3740. [PubMed: 35846392]
32. Zhao X; Chen G; Zhou Y; Nashalian A; Xu J; Tat T; Song Y; Libanori A; Xu S; Li S, Giant Magnetoelastic Effect Enabled Stretchable Sensor for Self-Powered Biomonitoring. Acs Nano 2022, 16 (4), 6013–6022. [PubMed: 35417654]
33. Xu J; Tat T; Zhao X; Zhou Y; Ngo D; Xiao X; Chen J, A Programmable Magnetoelastic Sensor Array for Self-Powered Human–Machine Interface. Applied Physics Reviews 2022, 9 (3), 031404.
34. Yao S; Zhu Y, Nanomaterial-Enabled Stretchable Conductors: Strategies, Materials and Devices. Adv. Mater 2015, 27 (9), 1480–1511. [PubMed: 25619358]
35. Ho MD; Ling Y; Yap LW; Wang Y; Dong D; Zhao Y; Cheng W, Percolating Network of Ultrathin Gold Nanowires and Silver Nanowires toward “Invisible” Wearable Sensors for Detecting Emotional Expression and Apexcardiogram. Adv. Funct. Mater 2017, 27 (25), 1700845.
36. Yao S; Yang J; Poblete FR; Hu X; Zhu Y, Multifunctional Electronic Textiles Using Silver Nanowire Composites. ACS Appl. Mater. Interfaces 2019, 11 (34), 31028–31037. [PubMed: 31373192]

37. Kim KK; Hong S; Cho HM; Lee J; Suh YD; Ham J; Ko SH, Highly Sensitive and Stretchable Multidimensional Strain Sensor with Prestrained Anisotropic Metal Nanowire Percolation Networks. Nano Lett. 2015, 15 (8), 5240–5247. [PubMed: 26150011]
38. Huang J; Zhou J; Luo Y; Yan G; Liu Y; Shen Y; Xu Y; Li H; Yan L; Zhang G, Wrinkle-Enabled Highly Stretchable Strain Sensors for Wide-Range Health Monitoring with a Big Data Cloud Platform. ACS Appl. Mater. Interfaces 2020, 12 (38), 43009–43017. [PubMed: 32856459]
39. Sun H; Dai K; Zhai W; Zhou Y; Li J; Zheng G; Li B; Liu C; Shen C, A Highly Sensitive and Stretchable Yarn Strain Sensor for Human Motion Tracking Utilizing a Wrinkle-Assisted Crack Structure. ACS Appl. Mater. Interfaces 2019, 11 (39), 36052–36062. [PubMed: 31498581]
40. Yan Z; Pan T; Wang D; Li J; Jin L; Huang L; Jiang J; Qi Z; Zhang H; Gao M, Stretchable Micromotion Sensor with Enhanced Sensitivity Using Serpentine Layout. ACS Appl. Mater. Interfaces 2019, 11 (13), 12261–12271. [PubMed: 30807090]
41. Gao Y; Guo F; Cao P; Liu J; Li D; Wu J; Wang N; Su Y; Zhao Y, Winding-Locked Carbon Nanotubes/Polymer Nanofibers Helical Yarn for Ultrastretchable Conductor and Strain Sensor. Acs Nano 2020, 14 (3), 3442–3450. [PubMed: 32149493]
42. Li C; Cui Y-L; Tian G-L; Shu Y; Wang X-F; Tian H; Yang Y; Wei F; Ren T-L, Flexible Cnt-Array Double Helices Strain Sensor with High Stretchability for Motion Capture. Sci. Rep 2015, 5 (1), 1–8.
43. Sun R; Zhang B; Yang L; Zhang W; Farrow I; Scarpa F; Rossiter J, Kirigami Stretchable Strain Sensors with Enhanced Piezoelectricity Induced by Topological Electrodes. Appl. Phys. Lett 2018, 112 (25), 251904.
44. Wu C; Wang X; Lin L; Guo H; Wang ZL, Based Triboelectric Nanogenerators Made of Stretchable Interlocking Kirigami Patterns. Acs Nano 2016, 10 (4), 4652–4659. [PubMed: 27058268]
45. Jiang Y; Liu Z; Matsuhisa N; Qi D; Leow WR; Yang H; Yu J; Chen G; Liu Y; Wan C; Liu Z; Chen X, Auxetic Mechanical Metamaterials to Enhance Sensitivity of Stretchable Strain Sensors. Adv. Mater 2018, 30 (12), 1706589.
46. Kang D; Pikhitsa PV; Choi YW; Lee C; Shin SS; Piao L; Park B; Suh K-Y; Kim T.-i.; Choi M, Ultrasensitive Mechanical Crack-Based Sensor Inspired by the Spider Sensory System. Nature 2014, 516 (7530), 222–226. [PubMed: 25503234]
47. Atalay O; Atalay A; Gafford J; Wang H; Wood R; Walsh C, A Highly Stretchable Capacitive-Based Strain Sensor Based on Metal Deposition and Laser Rastering. Adv. Mater.Technol 2017, 2 (9), 1700081.
48. Lee J; Shin S; Lee S; Song J; Kang S; Han H; Kim S; Kim S; Seo J; Kim D, Highly Sensitive Multifilament Fiber Strain Sensors with Ultrabroad Sensing Range for Textile Electronics. Acs Nano 2018, 12 (5), 4259–4268. [PubMed: 29617111]
49. Jeong YR; Park H; Jin SW; Hong SY; Lee SS; Ha JS, Highly Stretchable and Sensitive Strain Sensors Using Fragmentized Graphene Foam. Adv. Funct. Mater 2015, 25 (27), 4228–4236.
50. Shi C; Zou Z; Lei Z; Zhu P; Nie G; Zhang W; Xiao J, Stretchable, Rehealable, Recyclable, and Reconfigurable Integrated Strain Sensor for Joint Motion and Respiration Monitoring. Research 2021, 2021, 9846036. [PubMed: 34396138]
51. Dorsey ER; Bloem BR, The Parkinson Pandemic—a Call to Action. JAMA neurology 2018, 75 (1), 9–10. [PubMed: 29131880]
52. Monje MH; Foffani G; Obeso J; Sánchez-Ferro Á, New Sensor and Wearable Technologies to Aid in the Diagnosis and Treatment Monitoring of Parkinson's Disease. Annual review of biomedical engineering 2019, 21, 111–143.
53. Deuschl G; Krack P; Lauk M; Timmer J, Clinical Neurophysiology of Tremor. Journal of clinical neurophysiology 1996, 13 (2), 110–121. [PubMed: 8849966]
54. Xu F; Zhu Y, Highly Conductive and Stretchable Silver Nanowire Conductors. Adv. Mater 2012, 24 (37), 5117–5122. [PubMed: 22786752]
55. Liao Q; Mohr M; Zhang X; Zhang Z; Zhang Y; Fecht H-J, Carbon Fiber–Zno Nanowire Hybrid Structures for Flexible and Adaptable Strain Sensors. Nanoscale 2013, 5 (24), 12350–12355. [PubMed: 24162176]
56. Ma Y; Choi J; Hourlier-Fargette A; Xue Y; Chung HU; Lee JY; Wang X; Xie Z; Kang D; Wang H; Han S; Kang S-K; Kang Y; Yu X; Slepian MJ; Raj MS; Model JB; Feng X; Ghaffari R; Rogers JA,

Relation between Blood Pressure and Pulse Wave Velocity for Human Arteries. PNAS 2018, 115 (44), 11144–11149. [PubMed: 30322935]

57. Roy SH; De Luca CJ; Casavant DA, Lumbar Muscle Fatigue and Chronic Lower Back Pain. Spine 1989, 14 (9), 992–1001. [PubMed: 2528828]
58. Dankaerts W; O'Sullivan P; Burnett A; Straker L, Differences in Sitting Postures Are Associated with Nonspecific Chronic Low Back Pain Disorders When Patients Are Subclassified. Spine 2006, 31 (6), 698–704. [PubMed: 16540876]
59. Xia Y; Yang P; Sun Y; Wu Y; Mayers B; Gates B; Yin Y; Kim F; Yan H, One-Dimensional Nanostructures: Synthesis, Characterization, and Applications. Adv. Mater 2003, 15 (5), 353–389.
60. Yao S; Cui J; Cui Z; Zhu Y, Soft Electrothermal Actuators Using Silver Nanowire Heaters. Nanoscale 2017, 9 (11), 3797–3805. [PubMed: 28134386]

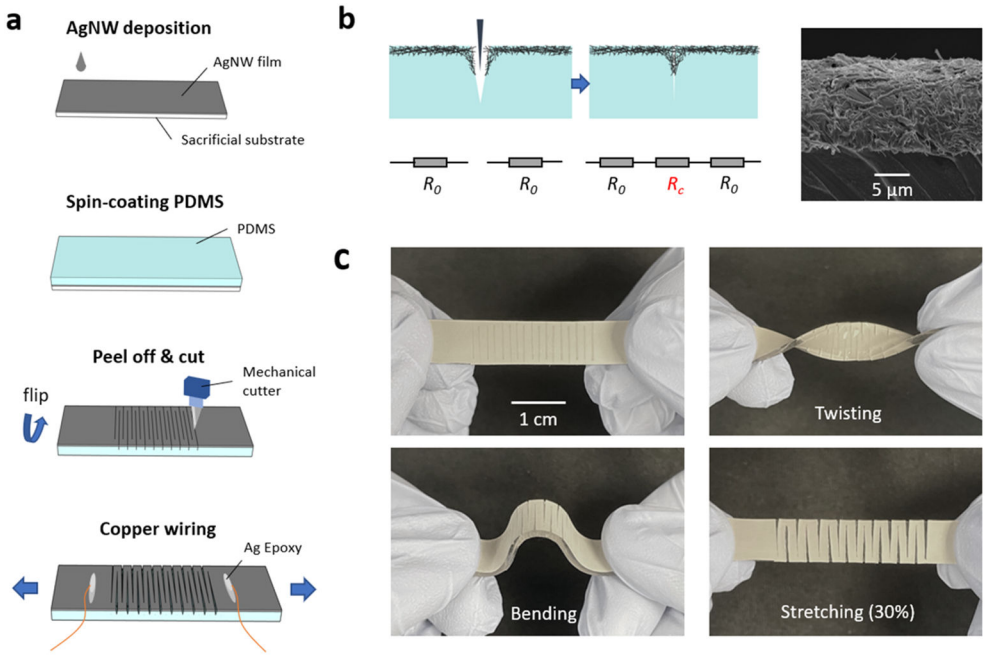


**Fig. 1. Overview of the soft stretchable strain sensor.**

**a,** Fabrication process of the sensor. **b**, Electrical model of the sensor during and after cuts. The SEM image shows the cross-section view of one cut surface. **c**, The undeformed sensor and the sensor under twisting, bending and stretching.

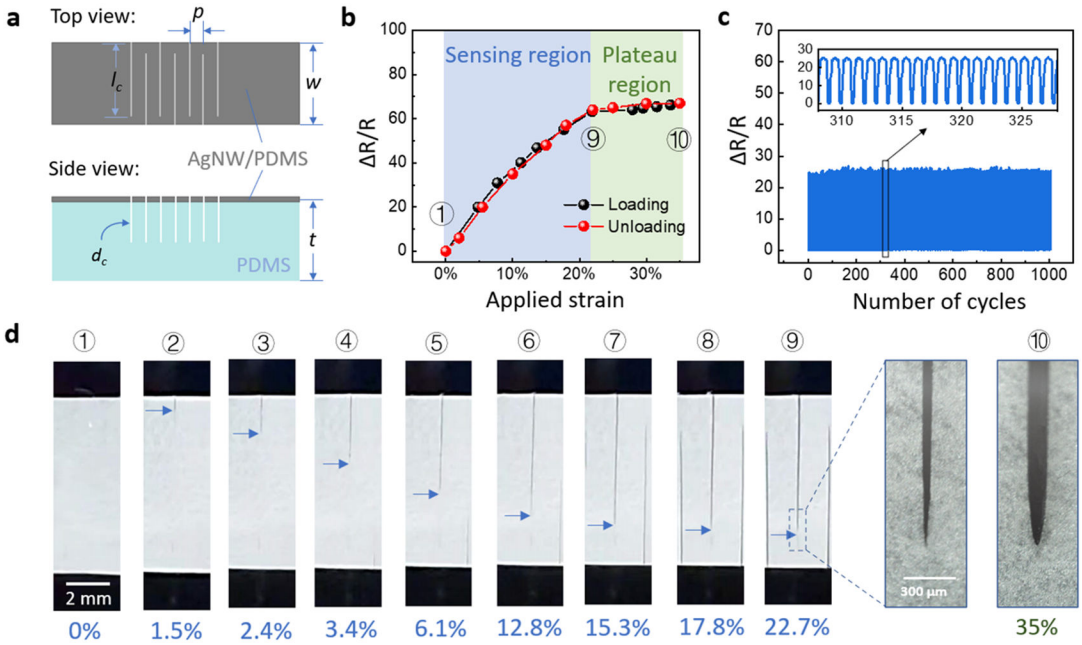


**Fig. 2. Electrical performances of the strain sensor under applied strain.**

**a,** Schematic of the sensor showing the pitch between cuts *p*, crack length $l_c$, specimen width *w*, cut depth $d_c$ and specimen thickness *t*. **b**, Resistance change of the sensor corresponding to snapshots in d**. c,** Sensor response to 1000 cycles of 30% applied strain. The inset figure shows 20 cycles. **d**, Snapshots of the top surface of the sensor under applied strain with magnified photographs showing the crack opening and tip blunting.

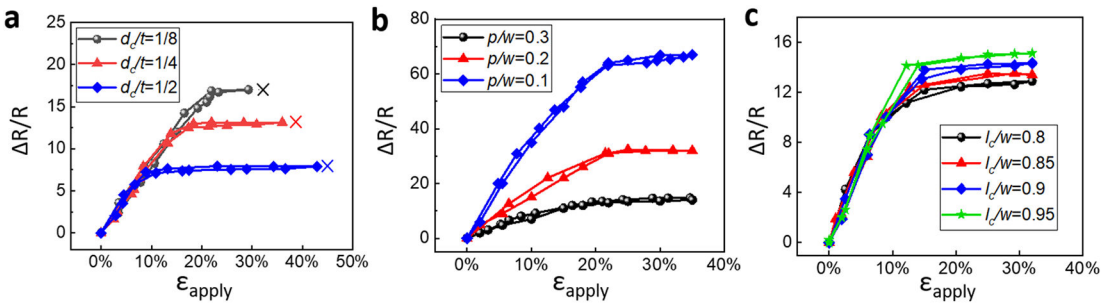


**Fig. 3. Geometrical design of the strain sensor.**

**a**, Resistance change of the sensors with $d_c/t$ = 1/8, 1/4, and 1/2 with respect to applied strain. Three cross markers with corresponding color represent the reversible range of each case from FEA. **b**, Resistance change of the sensors with $p/w$ = 0.1, 0.2 and 0.3 with respect to applied strain. **c**, Resistance change of the sensors with $l_c/w$ = 0.8, 0.85, 0.9 and 0.95 with respect to applied strain.

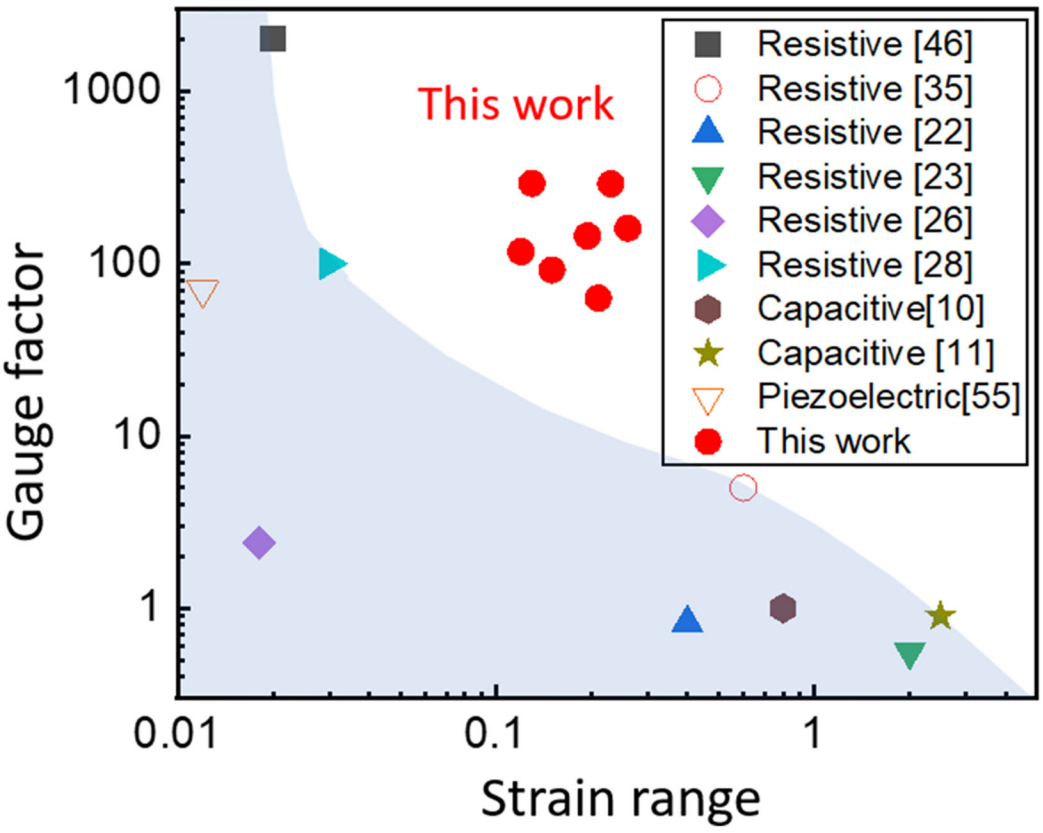


**Fig. 4. Performances of the strain sensors compared with the reported stretchable strain sensors.**

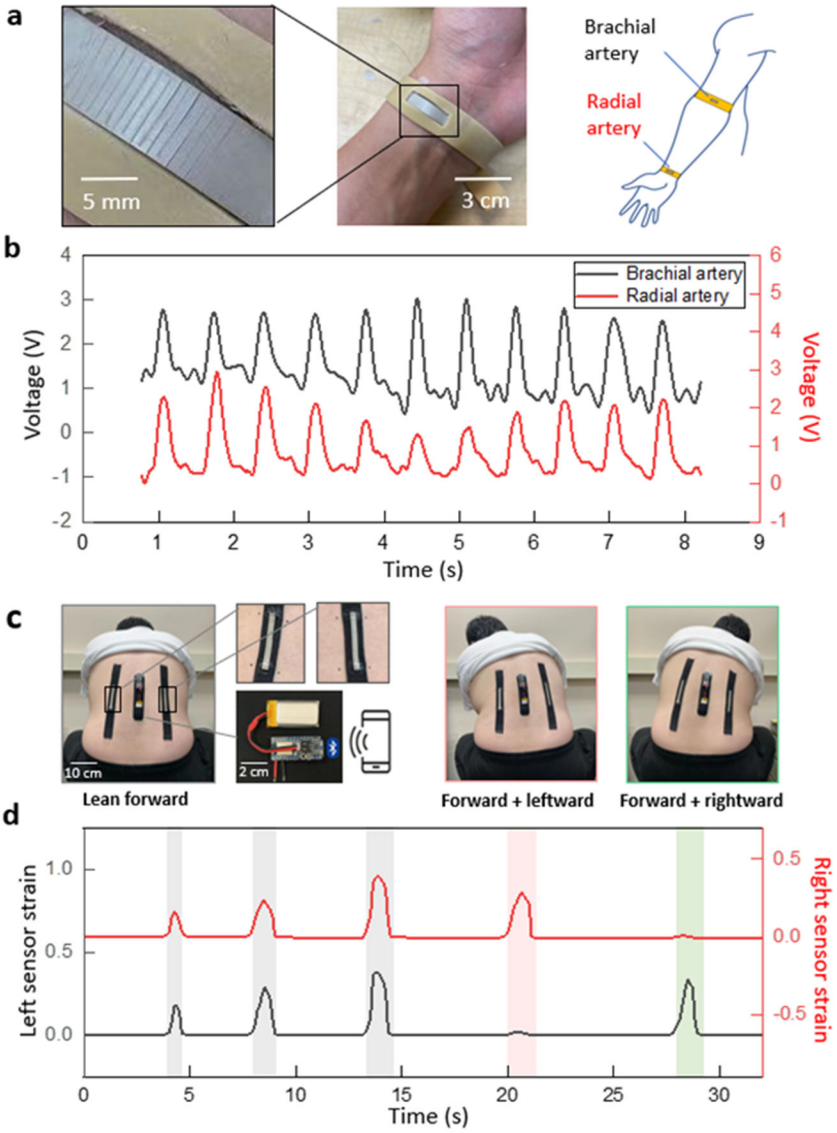


**Fig. 5. Demonstrations of the strain sensor for personal health monitoring.**

**a,** The sensor integrated with a wristband for monitoring blood pulse. **b**, Sensing results of two blood pulse sensors placed on the radial artery on the wrist and the brachial artery on the arm. **c**, Photographs of the sensor integrated with an athletic tape attached side by side along the spine for monitoring lower back strains. Inset shows the two sensors and the Bluetooth evaluation board for data collection and transmission. **d**, Sensing results of the two-sensor system detecting different bending motions of the lower back corresponding to photographs in **c**.

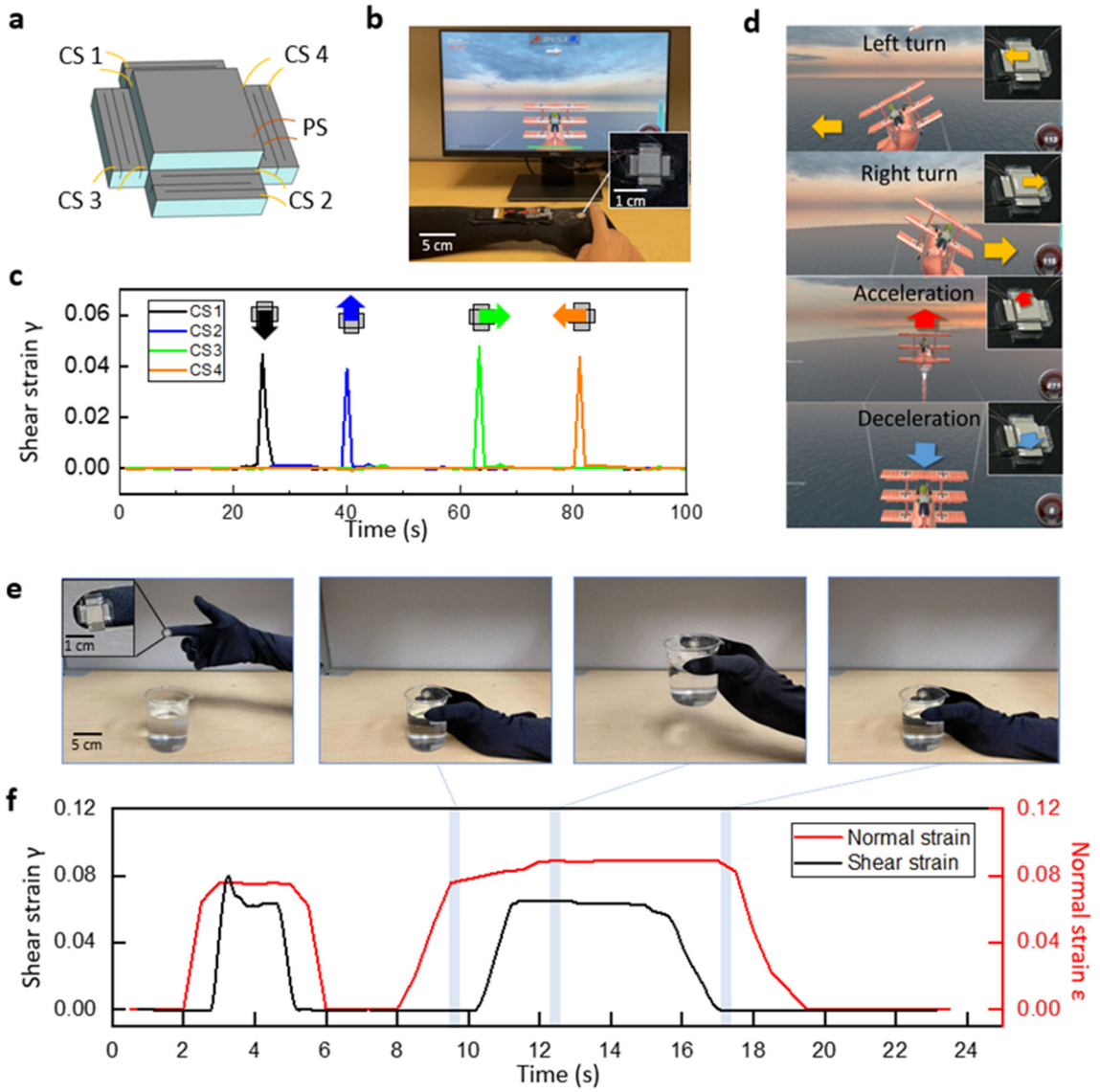


**Fig. 6. Demonstration of the strain sensor for human-machine interface and tactile sensing.**

**a,** Schematic layout of the 3D touch sensor consisting of a capacitive normal strain sensor and four shear strain sensors. **b**, Photograph of the 3D touch sensor connected to an evaluation board and laptop. Inset shows the 3D touch sensor. **c**, Shear strain of the touch sensor when pushing towards different directions using a finger. **d**, Application in playing an airplane video game. The four sensors correspond to four different functions: turning left, turning down, acceleration, and deceleration, respectively. **e**, Snapshots showing different stages of grasping a glass of water including grabbing, lifting and dropping. **f,** Shear strain and normal strain of the tactile sensor during two trials of grasping of the cup of water, showing the grabbing, lifting and dropping.